CrystEngComm

PAPER

Magnetic and structural correlations in [Fe(nsal$_2$trien)] salts: the role of cation–anion interactions in the spin crossover phenomenon†

Bruno J. C. Vieira, [iD] [a] Vasco da Gama, [iD] [a] Isabel C. Santos, [iD] [a] Laura C. J. Pereira, [iD] [a] Nuno A. G. Bandeira [iD] [bcd] and João C. Waerenborgh [iD] *[a]

We report the relevance of cation–anion and cation–solvent–anion interactions to the crystal lattice rigidity and the corresponding effect on the SCO behaviour of six Fe^{III} complexes with the hexadentate Schiff base ligand nsal$_2$trien. Four of these compounds were synthesized and structurally and magnetically characterized for the first time. In the most rigid structures, the SCO behaviour is either not allowed or severely hampered. For lower structural connectivity, incomplete transitions are observed within the 4–300 K temperature range. The most flexible structure shows a complete transition. The interactions between the cationic units and the anions were found to be more important than the cation–cation interactions for the SCO phenomenon and for the overall cooperativity related to the abrupt/gradual character of the transition. Computational studies were performed in order to determine the crystal splitting gap Δ_{oct}. The calculated values for the HS and LS Δ_{oct} are very similar for all compounds suggesting that these parameters have very little influence on the SCO behaviour.

Introduction

The spin crossover (SCO) phenomenon has been extensively studied due to its potential use in molecular electronics such as molecular memories or switches.[1] SCO can be found in a variety of 3d^4–3d^7 transition metal complexes and consists of the reversible transition between a high-spin (HS) and a low-spin (LS) configuration. The transition is triggered by a variation in temperature, pressure or magnetic field or by light irradiation. The SCO phenomenon induces changes in the physical properties of the material (crystal structure, magnetism, color, *etc.*) and may be monitored by several techniques.[1–3]

SCO transitions can be complete, incomplete, abrupt or gradual, in one step or in multiple steps. This variety is related to the way the structural changes induced by the SCO transition are propagated in the solid structure of each sys-

tem, *i.e.* the cooperativity between the SCO centres. This cooperativity can be understood as the sum of the contributions of a series of parameters correlated with the inter- and intramolecular interactions between the different molecules that constitute each system, cations, anions and solvating molecules. Other factors that contribute to the SCO transition such as the ligand field strength are well studied and the way the transition temperature depends on the ligand field is well established.[1] However, it has been proved difficult to make the same correlations with the intra- and intermolecular interactions due to the complexity of the arrangement of interactions that most structures exhibit.

The use of the [Fe(nsal$_2$trien)]$^+$ cation in our previous work[4] was mainly motivated by the expectation that extended cation–cation (DD) $\pi\pi$ interactions would lead to a strong cooperative behaviour (Fig. 1 shows a schematic representation of the H$_2$nsal$_2$trien ligand). It came to us as a surprise that, in spite of the large extended π system of the nsal$_2$trien ligand, no significant $\pi\pi$ interactions were observed in the [Fe(nsal$_2$trien)$_2$]SCN compound.[4] This unexpected result was

[a] Centro de Ciências e Tecnologias Nucleares (C2TN), Instituto Superior Técnico, Universidade de Lisboa, 2695-066 Bobadela LRS, Portugal.
E-mail: jcarlos@ctn.tecnico.ulisboa.pt
[b] Institute of Chemical Research of Catalonia (ICIQ), Avda. Països Catalans, 16-43007 Tarragona, Spain
[c] Centro de Química Estrutural – Instituto Superior Técnico, Universidade de Lisboa, Av. Rovisco Pais, 1049-001 Lisboa, Portugal
[d] Centro de Química e Bioquímica – Faculdade de Ciências, Universidade de Lisboa, Campo Grande, 1749-016 Lisboa, Portugal

† Electronic supplementary information (ESI) available: Crystallographic tables, figures of compounds and Hirshfeld plots. CCDC 1570257 (**1** at 150 K), 1570258 (**2** at 150 K), 1570259 (**3** at 150 K) and 1570256 (**4** at 150 K). For ESI and crystallographic data in CIF or other electronic format see DOI: 10.1039/c8ce00275d
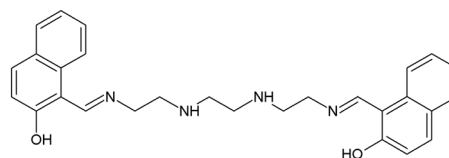

Fig. 1 H$_2$nsal$_2$trien.

further reinforced by the fact that in the only other known example of a salt with the same cation, $[Fe(nsal_2trien)]PF_6$ ·$(CH_3CH_2)_2O$,[5] $\pi\pi$ interactions were also absent. Although the latter compound presents the onset at ~250 K of what appears to be a gradual SCO phenomenon, $[Fe(nsal_2trien)]SCN$ displays a rather singular 2-step SCO behaviour, with a sharp low-temperature (142 K) transition and a rather gradual high-temperature (~250 K) SCO process.[4] SCO cooperativity has therefore been observed in compounds such as $[Fe(nsal_2trien)]SCN$ where DD interactions are weak in spite of the fact that it has been best understood and therefore mostly pursued when strong DD interactions are present. Besides the uncommon features displayed by the SCO behaviour of $[Fe(nsal_2trien)]SCN$, we were also motivated by the interesting properties of the $[Fe(sal_2trien)]^+$ described in ref. 7b and by the unpredictability of the spin-state behaviour of the $[Fe(nsal_2trien)]^+$ derivatives,[5,7a,b] hoping to relate the distribution and strength of the intermolecular interactions with the lattice flexibility/rigidity. With this motivation, we decided to study the SCO behaviour and its relation to the crystal packing in a series of salts based on the $[Fe(nsal_2trien)]^+$ cation.

In this paper, we report the synthesis and structural and magnetic characterization of four new salts, $[Fe(nsal_2trien)]Cl$ ·H_2O·CH_3CH_2OH (1), $[Fe(nsal_2trien)]ClO_4$ (2), $[Fe(nsal_2trien)]$-BF_4 (3) and $[Fe(nsal_2trien)]BPh_4$ (4). Their crystal packing and SCO behaviour are correlated with those of $[Fe(nsal_2trien)]PF_6$ ·$(CH_3CH_2)_2O$ (ref. 5) (5) and $[Fe(nsal_2trien)]SCN$ (ref. 4) (6). Computational calculations were also performed in order to determine the energy gap between the t_{2g} and e_g subsets of orbitals, often referred to as the ligand field splitting, for all compounds in order to determine possible differences in these values that might be related to their SCO behaviour.

Experimental details

Synthesis

Commercial solvents were used without further purification unless otherwise stated. The purity of the crystallized compounds and their solvation state were checked by determining the carbon, hydrogen, nitrogen and sulfur content at the C2TN elemental analysis service.

Preparation of $[Fe(nsal_2trien)]Cl \cdot CH_3CH_2OH \cdot H_2O$ (1). A methanolic solution (30 mL) of 2-hydroxy-1-naphthaldehyde (10 mmol, 1721.80 mg) was added dropwise to a methanolic solution (30 mL) of triethylenetetramine (5 mmol, 731.17 mg). The yellowish mixture was stirred at reflux temperature for 30 min. Then, a solution of sodium methoxide (10 mmol, 540.24 mg) in methanol (10 mL) was added to the mixture, turning its color to orange. After 30 min of stirring, iron(III) chloride (5 mmol, 811.012 mg) dissolved in methanol (30 mL) was added dropwise, and the mixture turned black. The volume was reduced to 50 ml and the mixture was cooled to −20 °C overnight. A dark solid was recovered by filtration and washed with cold methanol (2093.80 mg, 3.85 mmol). Yield: 77%. Dark green crystals were obtained *via* slow elution of diethyl ether into a concentrated solution of ethanol. Elem anal. calcd: C, 59.27; H, 5.97; N, 9.22. Found: C, 59.12; H, 5.95; N, 9.30%.

Preparation of $[Fe(nsal_2trien)]ClO_4$ (2). An aqueous solution (10 ml) of $NaClO_4$ (1.0 mmol, 122.44 mg) was slowly added to an aqueous solution of 1 (0.5 mmol, 303.96 mg) dropwise. The addition was performed over a period of 5 minutes. After the addition was completed, the solution was left unstirred for another 5 minutes at room temperature. The mixture was then cooled to 4 °C for 12 hours. A bulk green solid was collected by filtration and washed with cold diethyl ether (0.455 mmol, 276.57 mg). Yield: 91%. Dark green crystals were obtained by slow evaporation of a saturated methanol solution. Elem anal. calcd: C, 55.33; H, 4.64; N, 9.22. Found: C, 55.87; H, 4.96; N, 9.07%.

Preparation of $[Fe(nsal_2trien)]BF_4$ (3). An aqueous solution (10 ml) of $NaBF_4$ (1.0 mmol, 109.79 mg) was slowly added to an aqueous solution of 1 (0.5 mmol, 303.96 mg) dropwise. The addition was performed over a period of 5 minutes. After the addition was completed, the solution was left unstirred for another 5 minutes at room temperature. The mixture was then cooled to 4 °C for 12 hours. A bulk green solid was collected by filtration and washed with cold diethyl ether (0.465 mmol, 276.77 mg). Yield: 93%. Dark green crystals were obtained by slow evaporation of a saturated methanol solution. Elem anal. calcd: C, 56.50; H, 4.74; N, 9.41. Found: C, 56.29; H, 4.82; N, 9.35%.

Preparation of $[Fe(nsal_2trien)]BPh_4$ (4). A methanolic solution (10 ml) of $NaBPh_4$ (1.0 mmol, 109.79 mg) was slowly added to an aqueous solution of 1 (0.5 mmol, 303.96 mg) dropwise. The addition was performed over a period of 5 minutes. After the addition was completed, the solution was left unstirred for another 5 minutes at room temperature. The mixture was then cooled to −20 °C for 12 hours. A bulk green solid was collected by filtration and washed with cold diethyl ether (0.425 mmol, 371.74 mg). Yield: 93%. Dark green crystals were obtained *via* slow elution of diethyl ether into a concentrated solution of acetone. Elem anal. calcd: C, 75.46; H, 5.85; N, 6.77. Found: C, 75.04; H, 6.07; N, 6.55%.

In solution, all the compounds showed a green–brown colour variation at ~323 K consistent with equilibria between LS and HS states of the cations. A similar behaviour was reported for 5 in CD_3Cl solution with a $T_{1/2}$ value of ~332 K.[5]

Caution! Although we experienced no problems in handling the perchlorate salts in this study, metal–organic perchlorates are potentially explosive and should be handled with due care in small quantities.

X-ray crystallography

A summary of the crystal data, experimental details and refinement results is listed in Table 1, while selected bond distances and angles are presented in Table 2. The X-ray diffraction (XRD) experiments were performed at 150 K with a Bruker AXS APEX CCD detector four-circle diffractometer using a graphite-monochromated Mo Kα radiation source (λ

Table 1 Crystallographic data for compounds **1**–**4** at 150 K

	1 (150 K)	**2** (150 K)	**3** (150 K)	**4** (150 K)
Crystal size (mm)	0.16 × 0.12 × 0.10	0.14 × 0.10 × 0.04	0.30 × 0.22 × 0.16	0.20 × 0.10 × 0.06
Crystal colour, shape	Black, prism	Black, plate	Black, prism	Black, prism
Formula	$C_{30}H_{36}FeN_4O_4Cl$	$C_{28}H_{28}FeN_4O_6Cl$	$C_{28}H_{28}FeN_4O_2F_4B$	$C_{52}H_{48}FeN_4O_2B$
Molecular mass	607.93	607.84	595.20	827.62
Crystal system	Monoclinic	Orthorhombic	Orthorhombic	Monoclinic
Space group (no.)	$P2_1/n$	$Pbca$	$Pbca$	$P2_1/n$
a (Å)	8.6116(3)	16.7007(7)	16.4142(3)	14.960(2)
b (Å)	15.4474(4)	15.1105(8)	15.1139(4)	17.100(3)
c (Å)	20.4760(6)	20.7773(11)	20.9988(6)	17.112(3)
β (Å)	96.769(2)			110.277(9)
V (Å^3)	2704.87(14)	5243.3(4)	5209.4(2)	4106.3(11)
Z, $D_{calcd.}$ (mg m^{-3})	4, 1.493	8, 1.540	8, 1.518	4, 1.339
μ (mm^{-1})	0.702	0.729	0.643	0.416
$F(000)$	1276	2520	2456	1740
Theta range (deg)	2.72 to 25.03	2.67 to 25.68	2.67 to 25.03	2.53 to 26.37
Index range (h, k, l)	−10/10, −18/18, −24/23	−18/20, −17/18, −24/25	−19/19, −13/17, −24/24	−18/18, −21/21, −20/21
Refl. collected/unique	20 854/4760 [R_{int} = 0.0509]	25 058/4975 [R_{int} = 0.1203]	34 759/4596 [R_{int} = 0.0691]	34 004/8393 [R_{int} = 0.0629]
T max./min.	0.9332/0.8960	0.9714/0.9048	0.9041/0.8306	0.9755/0.9215
Goodness-of-fit on F^2	1.066	0.930	1.043	1.025
Final R_1 [$I > 2\sigma(I)$]/wR_2	0.0422/0.1172	0.0527/0.1055	0.0331/0.0762	0.0430/0.0892

= 0.71073 Å) in ψ and ω scan modes. A semi-empirical absorption correction was carried out using SADABS.[8]

Data collection, cell refinement, and data reduction were performed with the SMART and SAINT programs.[9] Structures were solved by direct methods using SIR97 (ref. 10) and refined by full-matrix least-squares methods using the program SHELXL97 (ref. 11) and a WINGX software package.[12] Non-hydrogen atoms were refined with anisotropic thermal parameters, whereas H atoms were placed in idealized positions and allowed to refine riding on the parent C atom. Molecular graphics were prepared using MERCURY.[13] In compound **1**, three of the refined interatomic distances, one O–H within a solvent molecule and two H–H between solvent and anion molecules, were found to be too large or too short, respec-

tively (CCDC 1570257). This is due to disorder in the arrangement of solvent molecules within the crystal structure. In the other compounds where no solvent is incorporated, all the refined distances were found to be accurate.

Magnetic characterization

Magnetic measurements on compounds **1** and **2** were performed on a S700X SQUID magnetometer with a 7 T magnet (Cryogenic Ltd.) using polycrystalline samples. The temperature dependences of the magnetic susceptibility of **1** and **2**, in the temperature range 5–320 K, were measured in step mode under magnetic fields of 2 and 1 T, respectively. Magnetic measurements on compounds **3** and **4** in the temperature range 10–390 K were performed on a SQUID MPS magnetometer with a 5.5 T magnet (Quantum Design, Inc.), with an applied magnetic field of 1 T for compound **3** and 2 T for compound **4**.

For each experimental point, the temperature of the sample was stabilized for at least 5 min. The paramagnetic susceptibility was deduced from the experimental magnetization data after the diamagnetism corrections were estimated from the tabulated Pascal constants. The values for the diamagnetic susceptibilities of **1**, **2**, **3**, and **4** were −597.6 × 10^{-6} emu mol^{-1}, −607.8 × 10^{-6} emu mol^{-1}, −611.2 × 10^{-6} emu mol^{-1}, and −827.6 × 10^{-6} emu mol^{-1}, respectively.

Computational details

The ORCA (ref. 14) program system was employed for all calculations presented herein. The B3LYP*[15] density functional was used employing Ahlrichs split valence basis sets (def2-SVP) with an additional polarisation function[16] for all non-metal atoms while the triple-zeta augmented variant (def2-TZVP) was used for iron. The chain-of-spheres resolution of the identity density fitting technique (RIJCOSX) was

Table 2 Selected bond lengths [Å] and angles [deg] for compounds **1**–**4**

	1 (150 K)	**2** (150 K)	**3** (150 K)	**4** (150 K)
Fe1–O1	1.895(2)	1.910(3)	1.9160(15)	1.8752(15)
Fe1–O2	1.885(2)	1.913(3)	1.9176(15)	1.8807(14)
Fe1–N1	1.920(2)	2.095(3)	2.0971(17)	1.9294(16)
Fe1–N2	1.997(2)	2.186(3)	2.184(2)	1.9916(19)
Fe1–N3	1.995(2)	2.169(3)	2.1745(18)	2.0014(19)
Fe1–N4	1.914(2)	2.111(3)	2.1054(17)	1.9273(16)
O1–Fe1–O2	95.67(9)	103.75(11)	104.13(7)	95.47(7)
O1–Fe1–N1	92.45(9)	85.54(11)	85.96(7)	91.75(7)
O2–Fe1–N1	88.41(10)	95.88(11)	94.98(6)	89.05(6)
O1–Fe1–N2	174.22(10)	157.40(11)	157.26(7)	173.48(7)
O2–Fe1–N2	88.41(10)	92.82(12)	92.83(7)	89.88(7)
N1–Fe1–N2	83.98(10)	77.45(12)	77.45(7)	84.58(8)
O1–Fe1–N4	87.55(9)	95.13(11)	94.76(7)	90.36(7)
O2–Fe1–N4	91.48(9)	85.04(11)	85.01(6)	92.51(6)
N1–Fe1–N4	179.90(12)	178.71(12)	179.26(7)	177.24(7)
N2–Fe1–N4	96.03(10)	101.62(11)	101.81(7)	93.15(7)
O1–Fe1–N3	91.62(10)	90.89(12)	90.39(7)	90.31(7)
O2–Fe1–N3	171.53(9)	158.31(11)	158.38(7)	173.34(8)
N1–Fe1–N3	95.58(10)	101.20(12)	102.05(7)	94.10(7)
N2–Fe1–N3	84.22(10)	78.13(12)	78.19(7)	84.59(8)
N4–Fe1–N3	84.52(10)	77.69(12)	77.79(7)	84.12(7)

employed in the calculations.[17] For orbital gap evaluations, the restricted open shell Kohn–Sham formalism[18] was employed using the unoptimised crystal structure geometries of the cationic complexes in their respective ground states. Free energy evaluations of the spin state structures and minimum energy crossing points[19] (MECPs) were carried out adding Grimme's third-generation dispersion correction[20] with the Becke–Johnson damping function[21] on top of the exchange–correlation functional (B3LYP*-D3) using the above basis set. An effective Hessian of the MECPs was obtained by a default procedure of displacing the coordinates along the crossing surface seam. Subsequent single-point re-evaluations of the electronic energy for each system were performed using a triple-zeta basis set augmented with two polarisation functions on every atom (def2-TZVPP) and a 5-digit grid integration accuracy (Grid5) without RI density fitting. These electronic energies were then summed to the sums previously obtained with the composite scheme in this manner:

$$G = E_{\text{el(def2-TZVPP)}} + \text{ZPE}_{\text{def2-TZVP+def2-SVP}} + E_{\text{vib(def2-TZVP+def2-SVP)}}$$
$$+ E_{\text{rot(def2-TZVP+def2-SVP)}} + E_{\text{trans(def2-TZVP+def2-SVP)}} + k_B T$$
$$- \text{TS}_{\text{(def2-TZVP+def2-SVP)}}$$

Results and discussion

Magnetization data

The temperature dependence of χT (where χ is the paramagnetic susceptibility and T is the temperature) for compounds **1–4** and **6** is shown in Fig. 2. The χT vs. T curve for **5** (ref. 5) is very similar to that for compound **4**. In agreement with XRD data, compounds **2** and **3** are purely HS exhibiting a nearly constant χT value of 4.56 and 4.63 emu K mol^{-1}, which is typical of HS Fe$^{\text{III}}$. Compounds **1** and **5** are essentially LS with χT nearly constant up to 200 K with values of the order of 0.5 emu K mol^{-1}. In the case of **4**, χT starts to increase
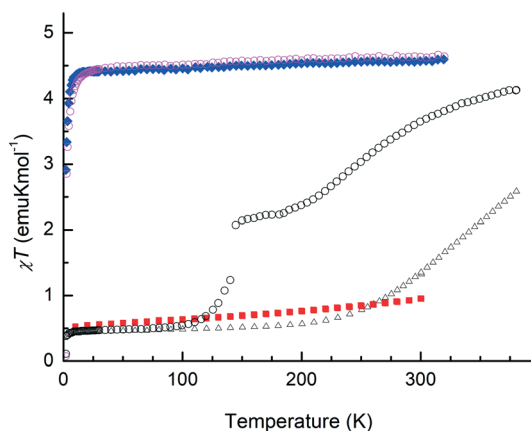

Fig. 2 Thermal dependence of χT for **1** (red squares, smaller symbols refer to measurements on cooling after heating up to 390 K), **2** (blue diamonds), **3** (open purple circles), **4** (open black triangles) and **6** (open black circles). The curve for **5** (ref.5) (measured up to 300 K) is very similar to the curve for **4**.

slightly above 200 K and above 250 K it is possible to observe the onset of a SCO process. At the highest temperatures achieved ($T \sim 390$ K), this process is still far from completion and the observed χT values indicate a HS fraction of $\sim 50\%$ calculated considering the average χT_{LS} and χT_{HS} values deduced from the low-temperature data of **4** and from the data of **2** and **3**, respectively.

Structural characterization

Table 1 presents the most relevant parameters for the single crystal determination. Compound **1** crystallizes in the monoclinic space group $P2_1/n$. Its asymmetric unit contains one [Fe(nsal$_2$trien)]$^+$ cation, one Cl$^-$ anion, one ethanol molecule and one water molecule, all in general crystallographic positions. Compounds **2** and **3** are isostructural crystallizing in the orthorhombic system, space group $Pbca$. Their asymmetric units contain one [Fe(nsal$_2$trien)]$^+$ cation and one anion, ClO$_4^-$ and BF$_4^-$, in **2** and **3**, respectively, in general positions. Compound **4** crystallizes in the monoclinic space group $P2_1/n$. Its asymmetric unit contains a single formula unit with one cation and one BPh$_4^-$ anion.

In compounds **1–4**, the coordination of the Fe$^{\text{III}}$ centres by the hexadentate nsal$_2$trien ligands consists of distorted octahedral environments with a *cis*-N$_4$O$_2$ coordination where the N$_{\text{imine}}$ atoms are in *trans* positions and the O and N$_{\text{amine}}$ are in *cis* configurations. Selected bond lengths and angles of the first coordination sphere of the [Fe(nsal$_2$trien)]$^+$ cations are summarized in Table 2. The interatomic distances increase in the order Fe–O < Fe–N$_{\text{imine}}$ < Fe–N$_{\text{amine}}$ and these distances are found to be significantly larger in **2** or **3** than in **1** and **4**. In the case of **2** and **3**, the Fe–O and Fe–N distances are within the range observed for fully HS configuration in related complexes.[4,5,22] In **1** and **4**, those distances are consistent with the reported values for LS complexes with this kind of ligand.[4,5,22] The assignment of LS and HS states in these four compounds is in good agreement with the magnetization data described above.

The octahedral distortion of these complexes and the correlations with the spin states have been evaluated on the basis of the parameters Σ and θ. The former parameter quantifies the angular deviation from an ideal octahedral geometry and the latter indicates the distortion from an octahedral towards a trigonal prismatic geometry, both indices being 0 for an ideal octahedron.[7a] The obtained parameters are presented in Table 3, along with those from the HS and LS phases of the related compounds [Fe(nsal$_2$trien)]PF$_6$·(CH$_3$CH$_2$)$_2$O (ref. 5) (**5**) and [Fe(nsal$_2$trien)]SCN (ref. 4) (**6**). As expected, the HS complexes exhibit significantly larger deviations ($84 < \Sigma < 97°$ and $233 < \theta < 249°$) from the ideal octahedral geometry than the LS forms of the complexes ($35 < \Sigma < 63°$ and $66 < \theta < 151°$). Furthermore, Σ and θ are maximal for the compounds that remain HS in the 4–300 K temperature range. This behaviour is similar to that of HS [Fe(bpp)$_2$]$^{2+}$ derivatives where SCO becomes progressively rarer as the distortion of the octahedral coordination increases.[23]

Table 3 Summary of the parameters characterizing the octahedral distortion (Σ and θ) and ligand conformation distortions (τ and α) for compounds **1**–**6** (see text for definition of the parameters)

Compound	Conf. (phase)	Σ	θ	τ	α
1	LS (LS)	45.3	91	8.19; 9.73	76.46
4	LS (LS)	35.4	66	0.66; 19.27	83.44
5	LS (LS)	43.5	98	3.57; 23.69	61.83
6	LS (LS)	61.1	141	1.13; 22.49	114.63
6	LS (Int)	62.7	151	0.24; 20.4	111.72
6	HS (Int)	87.8	241	5.31; 14.95	115.75
6	HS (HS)	84.4	233	2.43; 13.1	112.97
2	HS (HS)	97.4	248	1.04; 4.44	98.03
3	HS (HS)	96.5	249	3.09; 5.09	96.32

In spite of the relative success in the observation of empirical correlations between the structural distortions and the magnetic behaviour of SCO compounds in Fe^{II} and Fe^{III} complexes,[7,24] these efforts have been unsuccessful when ligand conformation distortions are considered. These distortions are characterized by the dihedral angle α, which indicates the angle between the phenoxy "arms" in the complexes, and by the values of the Fe–O–C–C torsion angle τ (Table 3). In the case of the dihedral angle α, a significant dispersion of values is observed both in the LS and in the HS forms (61.8–114.6° and 96.3–115.8°, respectively) in the range of that previously observed for the [Fe(sal$_2$trien)]$^+$ derivatives (61.8–124.9°),[5] typically indicating a strong distortion relative to the ideal octahedral geometry (α = 90°). In some sense, these high distortions of the cations are only possible due to the energy gains resulting from the establishment of very strong cation–anion H bonds and cation–cation $\pi\pi$ interactions in comparison to the energy loss associated with the distortion of the cations. It should be stressed that, in particular for the [Fe(nsal$_2$trien)]X compounds, the highest distortion, as evaluated by the parameter α, was observed for **6**, the only compound that displays a complete SCO in the 4–400 K temperature range.

Supramolecular arrangements

The crystal structures of compounds **1**–**4** are based on alternating layers consisting of arrangements of parallel chains of [Fe(nsal$_2$trien)]$^+$ cations with strong pairwise $\pi\pi$ interactions along the chains through contacts between the aromatic phenoxy fragments of the nsal$_2$trien ligands. The anions A are located at the border of the cationic layers, establishing sizable contacts, mainly through strong NH···A hydrogen bonds, with the "diamino" fragments (–Et–NH–Et–NH–Et–) of the nsal$_2$trien ligands. Fig. S1† shows projections of the crystal structures of compounds **1**, **2** and **4**, viewed along the direction of the chains. In the case of **3**, which is isostructural to **2**, the corresponding projection can be seen in Fig. S2.†

These projections illustrate the arrangements of three layers in the crystal structures of these compounds, where one of the chains in each layer is shown in black, for a better identification. The chains are parallel to [100] in **2** and **3** and

to [101] in **4**, while in the case of **1**, the chains in alternating layers are parallel to [110] and [1$\bar{1}$0]. The angle between these directions is 58.1°. A detail of the arrangement of two chains in neighbouring layers of compound **1** is shown in Fig. S3.† In the case of **1**, the CH_3CH_2OH molecules are located in between the cationic chains within the layers, separating the chains, and the H_2O molecules are segregated to the border of the layers closer to the Cl^- anions.

For simplicity, hereafter, the interactions will be referred to as DD for cation–cation, AA for anion–anion and DA for cation–anion.

Within the chains of compounds **1**–**4**, $\pi\pi$ interactions are observed between the [Fe(nsal$_2$trien)]$^+$ cations via two distinct overlapping modes of the large aromatic systems of both phenoxy rings of the ligands. These two overlapping modes are referred to as I and II as they correspond to the shorter and longer intrachain separations, respectively. The arrangements of the cations within the chains are illustrated in Fig. 3, where the DD short contacts, shorter than the sum of the van der Waals radii, S_{vdW}, as well as the $\pi\pi$ contacts not
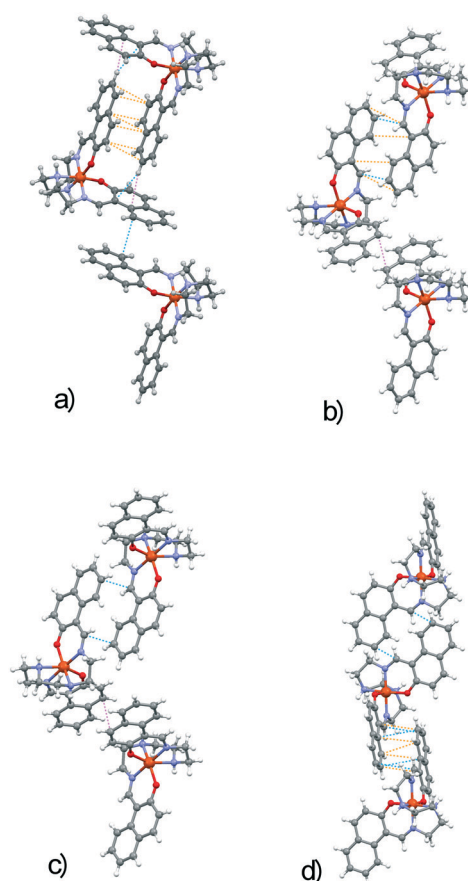

a)   b)

c)   d)

Fig. 3 Intrachain arrangement within the cationic chains and DD contacts ($\pi\pi$ contacts and CH···π hydrogen bonds) represented by the dashed lines, where the colour code of the contacts depends on $\Delta = d - S_{vdW}$ where d is the interatomic distance and S_{vdW} is the sum of the van der Waals radii in **1** (a), **2** (b), **3** (c) and **4** (d). Violet for $\Delta < -0.1$ Å, light blue for $\Delta < 0$, and orange for $\Delta < 0.1$ Å (only for $\pi\pi$ contacts). The DD contacts on the top correspond to overlap mode I and the ones on the bottom to mode II.

exceeding S_{vdW} by more than 0.1 Å, are shown as dashed lines.

Short separations, d_{LL}, are observed in both overlapping modes between the average plane of the two interacting phenoxy rings, clearly shorter than S_{vdW}, or shorter than 3.400 Å for the C···C contact. A significant longitudinal shift, d_{shift}, of the order of ~1.83–4.98 Å is observed in the overlapping between both aromatic systems of the interacting cations (Fig. S3†). The key parameters describing the intrachain overlapping modes, d_{LL} for both overlapping modes, d_{shift}, as well as the shortest distance between centroids of both aromatic systems, d_{cent} in 1–4, are summarized in Table S1.† The extent of the overlap between the π systems of the cations in 1, 2 and 3 is larger in overlap mode I than in II, as shown in Fig. S3† and by the d_{shift} and d_{cent} values in Table S1.† It appears however to be compensated by the smaller interplanar or interatomic distances of overlap II. In 4, which presents a slightly distinct intrachain arrangement, a much larger shift can be observed in overlap mode I, reflected on the significantly larger values of d_{shift}^I and d_{cent}^I. The smaller interplanar separation d_{LL} of this overlap suggests that the relative strength of both modes is not expected to differ substantially. Despite the differences in the various DD intrachain interactions, it seems reasonable to treat these chains as relatively rigid structural elements of the crystal lattices of this series of compounds. A more exhaustive list of the intrachain contacts, including those corresponding to the ππ contacts, lower than or not exceeding S_{vdW} by more than 0.1 Å (~3%), is summarized in Tables S2–S5.†

In addition to the strong intrachain DD ππ interactions, the [Fe(nsal₂trien)]⁺ cations of compounds 1–4 only present relatively weak direct DD interactions, mostly through CH···π interactions, with cations located in neighbouring chains either in the same layer in the case of 2 and 4 or in adjacent layers in the case of 1 and 3.

However, the strong interactions involving the anions and solvent molecules in the case of 1 assure an extended connectivity between the cations in the crystal structure of this compound.

In 2 and 3, the DA hydrogen bonds (Tables S2–S5†) provide a strong indirect DAD connectivity between pairs of [Fe(nsal₂trien)]⁺ cations located in neighbouring layers via NH···O–Cl–O···HN or NH···F–B–F···HN contacts, respectively, with short O···H separations of 2.118 and 2.169 Å and H···F separations of 2.134 and 2.275 Å. Additional weaker CH···O (in 2) and CH···F (in 3) hydrogen bonds also contribute to the DA interactions which play, therefore, a key role in the DD intralayer interchain coupling. In compound 1, the interlayer interchain coupling resembles that in 2 and 3, and a strong indirect DAD (NH···Cl···HN) connectivity between cations in neighbouring layers is observed with Cl···H separations of 2.193 and 2.310 Å (Tables S2–S5†). However, unlike what is observed in 2 and 3, in 1 the Cl⁻ anions are not directly involved in the intralayer interchain DD connectivity. In the absence of direct DD contacts in 1, the intralayer connectivity is mediated by strong hydrogen bonds between the

cations and the solvent molecules. The intralayer and interlayer connectivities in 1–4 are illustrated in Fig. 4 and 5, respectively, where the relevant molecules and contacts are shown.

The intralayer DD interactions in 4 are expected to be considerably stronger than those in compounds 1–3, due to the strong edge-to-face interactions (CH···π) between the π systems of the ligands in neighbouring chains within the layers. In 4, the direct DD contacts are significantly reinforced through the indirect DAD contacts which involve not only the cations that establish the direct DD contacts, shown in Fig. 4, but also the strong indirect DAD connectivity extending to two other neighbouring cations within the layer, which for the sake of simplicity are not included in Fig. 4.

Along with the DD ππ interactions which give rise to the cationic chains, the strong DA hydrogen bonds play a crucial
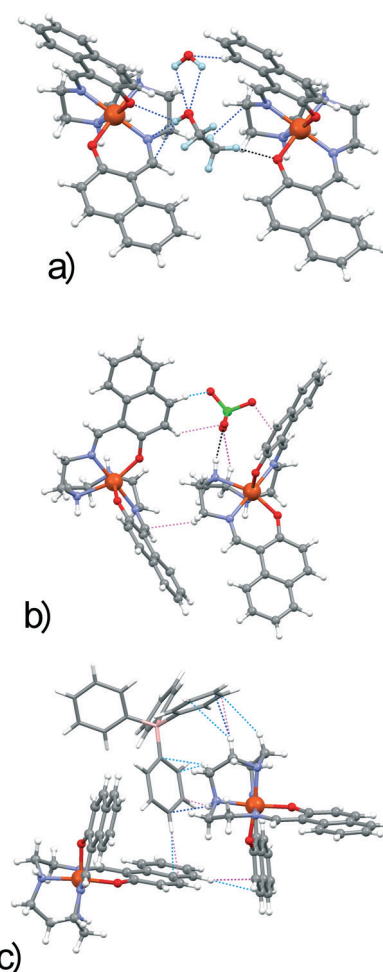

Fig. 4 View of the intralayer interchain DD connectivity in crystal structures of 1 (a), 2 (b) and 4 (c). As mentioned in the text, besides direct DD contacts, the overall connectivity is assisted by interactions with the anions in 2 and 4 or depends entirely on interactions mediated by the CH₃CH₂OH and H₂O solvent molecules in 1. Colour code of the contacts (with $\Delta = d - S_{vdW}$): black for $\Delta < -0.5$ Å; dark blue for $\Delta < -0.3$ Å; magenta for $\Delta < -0.2$ Å; violet for $\Delta < -0.1$ Å; light blue for $\Delta < 0$. For simplicity, contacts longer than those corresponding to $\Delta < -0.3$ Å were omitted in 1.
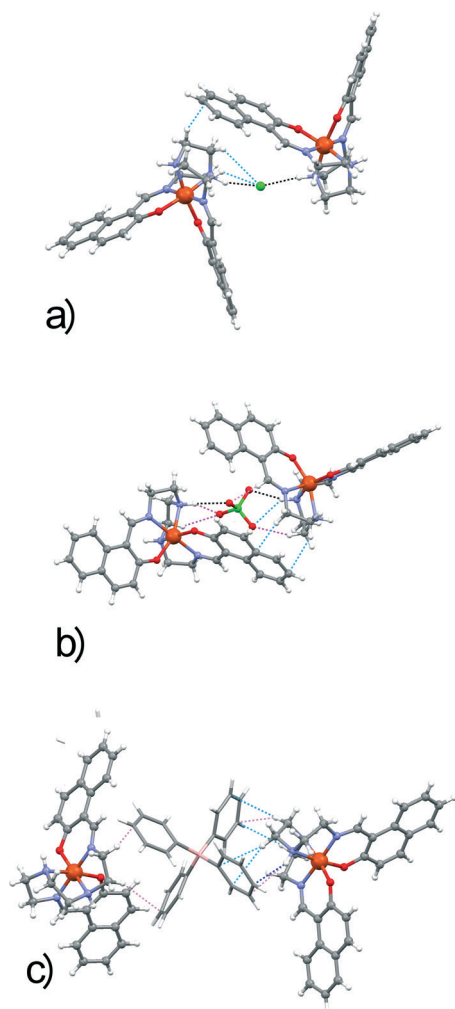
Fig. 5 View of the interlayer DD connectivity in crystal structures of **1** (a), **2** (b) and **4** (c). Colour code of the contacts as defined for Fig. 4.

role in the establishment of the crystal packing of these compounds. These strong DA interactions give rise to the existence of rigid stacks of alternating DA contacts, $\cdots D^1AD^2AD^1AD^1D^2\cdots$, in the borders of the layers, involving cations from one layer, D^1, and from the neighbouring one, D^2. This situation is distinct in **1**, where the small Cl^- anions only establish strong interactions with one H from each of the cations, which leads to a more flexible DAD arrangement, allowing a distinct orientation of the cations and the non-collinearity of the cationic chains in neighbouring layers. However, the interconnections between the anions, solvent molecules and the cations may compensate for the apparently more flexible DAD arrangement. In **4**, besides the fact that there are no direct DD contacts between cations in neighbouring layers, the indirect DAD connectivity (Fig. 5) is mediated through a flexible bridge between two phenyl groups ($D^1\cdots Ph$–B–$Ph\cdots D^2$). Although one of the interactions between the BPh_4^- anion and one of the cations corresponds to a strong $NH\cdots\pi$ contact, the second, associated with a $CH\cdots\pi$ contact, is considerably weaker. In spite of the slightly higher rigidity associated with the intralayer arrangement in

4, the much softer interlayer DAD connectivity is expected to lead to an increase in the overall lattice flexibility when compared to compounds **1**–**3**.

Correlation between the structure and magnetic behaviour

The SCO behaviour of these compounds shows a good correlation with that expected considering the flexibility/rigidity of the crystal packing. In **2** and **3**, obtained in the HS state and with the highest octahedral distortion (Σ and θ in Table 3), the lattice rigidity appears to lock the cations in this configuration, while in the case of **1** the cations are kept LS up to 300 K and in the case of **4** an incomplete SCO process is observed. A spin transition occurs in **4** where the deformation associated with the SCO process is expected to require less energy than it would in **1**.

The related compound **5** exhibits a SCO behaviour very similar to that observed in **4**. **5** is LS at low temperatures and presents the onset of a SCO process slightly above 200 K. At 300 K, the HS fraction is of the order of 15%,[5] only slightly lower than the value found for **4** (~20%).

The crystal structure of **5** is quite distinct from those of **1**–**4**. In **5**, the cations form strongly coupled pairs through a pair of short $NH\cdots\pi$ contacts and these pairs interact between themselves through weaker $CH\cdots\pi$ interactions, giving rise to layers of cations. No direct interlayer DD contacts are observed and the connectivity between the layers depends on the DA interactions. Each anion presents a quite strong interaction, a short $NH\cdots F$ hydrogen bond with one cation, and a few weaker $CH\cdots F$ contacts to other cations located either in the same layer or in neighbouring layers which ensures the interlayer connectivity. In **5**, the solvent $(CH_3CH_2)_2O$ molecules occupy vacancies in the cationic layers and their weak interactions with cations in neighbouring layers assist the indirect connectivity mediated by the anions.

The similitude of the SCO behaviour of this compound and of compound **4** suggests that the absence of strong DD $\pi\pi$ contacts and the consequent weakening of the rigidity within the cationic layers in **5** must be somehow compensated by the indirect DAD connectivity when compared with the soft connection involving the large deformable BPh_4^- anions in **4**.

Compound **6** exhibits a rare two-step SCO process with symmetry breaking.[4] Symmetry breaking SCO has been only observed in five Fe^{III} compounds.[4,6,25–27] Although not frequent, it is more common in Fe^{II}.[28] The clarification of this type of behaviour is still a major challenge in the general understanding of cooperative SCO processes. The two-step behaviour of compound **6** is characterized by an unusually high asymmetry in the progress of the spin transitions, one quite gradual at high temperatures and a second rather sharp denoting a much higher cooperativity. Although a slight decrease in the cooperativity in the higher temperature process is a common trend in two-step SCO compounds, the dramatic difference observed in **6** is quite unusual. In the case

of Fe^{III} compounds, a similar effect was only detected in two other compounds, [Fe(qsal)$_2$]SCN[29] and [Fe(qsal-F)$_2$]SCN.[30] Taking into consideration the correlations between the crystal packing and the SCO behaviour in the new [Fe(nsal$_2$trien)]$^+$-based compounds, the crystal structures of the three phases of **6** were reanalysed in greater detail in order to rationalize the peculiar behaviour observed.

The arrangement of the [Fe(nsal$_2$trien)]$^+$ cations and the anions in the crystal structure of **6** resembles those observed in **2** and **3**. The crystal structure of **6** is also based on alternating layers of parallel chains of cations that are held together by very strong DA interactions. A view of a projection of the crystal structure of **6** along the chain direction is shown in Fig. S4.†

The main difference in the case of **6** results from the linear geometry of the SCN$^-$ anion. This geometry causes a considerable tilting of the phenoxy rings of neighbouring cations (~32–36°) clearly deviating from the parallel face-to-face DD arrangement observed in the other compounds (Fig. S5†). In spite of the short intrachain DD separations, reflected by the shortest distance between one C atom and the average plane from a phenoxy ring in the neighbouring cation, d_{CL} (Table S1†), this large tilting is expected to severely weaken ππ interactions.

The weakness of the intrachain DD interactions in **6** allows the occurrence of a gradual spin transition centred at 250 K. However, the lattice does not seem to be flexible enough to accommodate the full conversion to the LS state and only half of the spins are converted, the transition to the Int phase appearing to be completed only at 220 K. As expected, the crystal structure of the Int phase at 150 K reveals a significant shortening of the intermolecular contacts, particularly those corresponding to the interlayer interactions, mostly the strong NH···S and ππ DA contacts, and to the intralayer interchain interactions, CH···π contacts, similar to those of **2** and **3**. The moderate strengthening of the intrachain DD interactions, mostly ππ and CH···π contacts, is not large enough to prevent the SCO process of the remaining HS cations, but significantly improves the cooperativity in the transition to the LS state that occurs as a sharp process at 142 K. In the Int phase, although the stronger direct DD interactions, CH···π interchain contacts, concern interactions between HS and LS cations, the DD interactions within the HS network are expected to be slightly stronger than those in the LS network. This subtle distinction concerning relatively weak interactions from CH···π and CH···O contacts of the order of S_{vdW} combined with the lattice thermal expansion seems to account for the distinct behaviours observed in the two steps of the SCO process of **6**. The DD contacts in the HS and LS networks of the Int phase are illustrated in Fig. S6 and S7.†

The evaluation of the lattice flexibility/rigidity in this series of compounds resulting from both the DA and DD interactions as well as from their arrangement in the crystal packing appears to correlate quite well with the SCO transition temperature, $T_{1/2}$, or the blocking of the HS state.

The intermolecular interactions in this series of compounds were also studied through Hirshfeld surface analysis.[31] This analysis essentially confirms the features already stressed in the above discussion, particularly concerning the stronger DD, DA and, in the case of **1** and **5**, DSolv interactions. The fingerprint plots for the [Fe(nsal$_2$trien)]$^+$ cations are shown in Fig. S8 and S9.† Resolved fingerprint plots concerning the most relevant DA (H···X, with X = Cl, O, F, C), DSolv (H···Y, with Y = O, C, H) and DD (C···C, H···C, H···H and H···O) interactions are also shown. These fingerprint plots map the (d_i, d_e) values, where d_i and d_e are the closest distances from each point of the Hirshfeld surface to the nearest nuclei external (d_e) and internal (d_i) to the surface.

The most relevant interactions correspond to the lowest values of d_i and d_e (bottom left quadrant of the plots). Besides the H···H contacts that are the dominant feature in the fingerprint plots, corresponding to 47–55% of the Hirshfeld surfaces, the strongest DA interactions (NH···Cl, NH···O, NH···F, NH···π, NH···S) emerge for low d_i values as spike-like patterns. The CC interactions, including the ππ ones, appear in the middle of the plot roughly for $d_i \sim d_e \geq 1.6$ Å, as arrow-like patterns for the compounds exhibiting ππ interactions (**1–4** and **6**). In **5**, the C···C contacts appear at higher $d_i \sim d_e > 1.8$ Å. Fig. S10† shows the resolved fingerprint plots of the C···C contacts for compounds **1–6** in the absence of the anions or solvent molecules, *i.e.* considering only DD interactions. This figure evidences that in **6** the projection from the arrow for lower (d_i, d_e) values ($d_i \sim d_e < 1.85$ Å) corresponds to DA interactions only, while the DD interactions, including the weakest ππ contacts of this compound, correspond to $d_i \sim d_e \sim 1.9$ Å, higher than those observed in **1–4**.

Computational studies

In order to unravel the interplay between the spin crossover phenomenon and the energetic positioning of the frontier orbitals, theoretical calculations were performed. The diversity of the magnetic behaviours observed in the title compounds makes them excellent candidates to study the correlation between the magnetic properties and the octahedral field splitting parameter (Δ_{oct}) value. Since the early days of SCO phenomenon studies, the Δ_{oct} parameter has been regarded as a defining factor for the occurrence of transition.[1] By means of density functional theory,[32] the energy eigenvalues of the one-electron orbitals can be quantified and assumed as a measure of the octahedral splitting parameter Δ_{oct} ($t_{2g} \rightarrow e_g^*$). The spin unrestricted Kohn–Sham (UKS) approach is generally adopted in open shell cases as it provides the best total energies for the system under examination. However, the effect of spin polarisation[33] stemming from this formalism results in considerable ligand admixing in the spin-up set of MOs while the metal orbitals are more prevalent in the spin-down set. Although some authors[34] choose the spin-down set for gap estimations, we chose the restricted open-shell Kohn–Sham (ROKS) formalism which sidesteps the issue of spin polarisation altogether. Therefore, Δ_{oct} is simply taken as the

Table 4 Δ_{oct} (eV) parameters of the cationic iron complexes calculated as the smallest energy difference between ROKS molecular orbitals with predominantly metallic character

Compound	Spin state	Δ_{oct} (eV)	$\Delta\varepsilon$
2	HS ($S = 5/2$)	1.027	SOMO$-3 \rightarrow$ SOMO-2
3	HS ($S = 5/2$)	1.003	
6	HS ($S = 5/2$)	1.067	
6	LS ($S = 1/2$)	5.110	SOMO $\rightarrow$ LUMO+2
1	LS ($S = 1/2$)	5.202	
4	LS ($S = 1/2$)	5.306	
5	LS ($S = 1/2$)	5.162	

Fig. 7 Sketch of the calculated free energies of the [Fe(nsal₂trien)]⁺ cation taking its ground state as the reference.

energy difference between the highest energy MO of the t_{2g} set and the lowest energy MO of the e_g^* set in both the HS and LS cases. Table 4 shows the calculated values pertaining to the cation geometries in the crystal structures. The well-established B3LYP* variant[15] of the B3LYP functional was chosen as the method of calculation.

The calculated values reveal a clear difference between the LS and HS structures as expected.[1] They are consistent with those reported for Fe in octahedral coordination. As far as we know, no values have been reported specifically for Fe(nsal₂trien) salts. Compounds in the LS state have higher values of Δ_{oct} when compared with HS structures in agreement with the metal–ligand distances. This difference is expected and reflects the variation of the electron population of the e_g anti-bonding orbitals.

In these structures, the values of Δ_{oct} range from 5.110–5.306 eV for the LS states and from 1.003 up to 1.067 eV for the HS states. **6**, the only compound in the present study which exhibits a full SCO transition in the 100–390 K temperature range, has the lowest LS value, 5.110 eV, and the highest HS value, 1.067 eV. It is not possible to propose a correlation between the calculated Δ_{oct} values and the magnetic behaviour of the compounds. In fact, the differences between the values calculated for each spin state are very small. Furthermore, the number of structures analysed is low and the LS or the HS values cannot be calculated by the present method for most compounds which are HS (**2**, **3**) or mainly LS (**1**, **4**, **5**), respectively, in the whole 4–390 K temperature range.

The dynamic process of spin-crossover of the [Fe(nsal₂trien)]⁺ cation was also computationally examined. The kinetics of this process is dictated by the crossing of po-
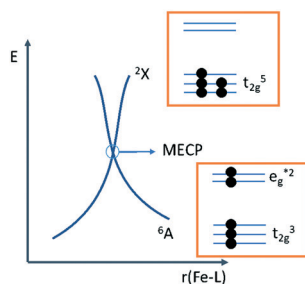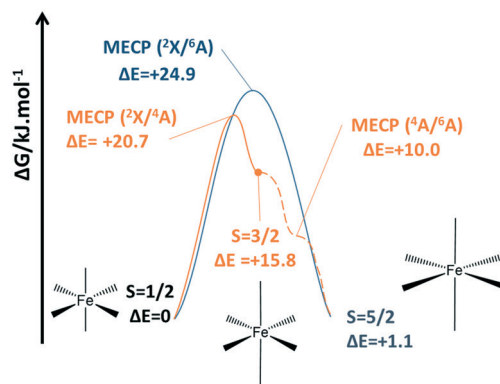
tential energy surfaces of the two spin states. Generally, the hopping of one surface to another is forbidden in light atoms but spin–orbit coupling can introduce off-diagonal couplings in the Hamiltonian mixing the states and thus allowing for an intersystem crossing. The lowest energy point in the intersection seam is generally known as the minimum energy crossing point[35] (MECP) (Fig. 6) and its thermal accessibility will govern the kinetics of spin crossover.

Herein, we adopt B3LYP*-D3/def2-TZVP+def2-SVP//B3LYP*-D3/def2-TZVPP as the computational protocol (see computational details).

MECPs were optimized for three intersections: between $S = 5/2$ and $S = 3/2$ (sextet and quartet, respectively), $S = 5/2$ and $S = 1/2$ and finally $S = 3/2$ and $S = 1/2$. These results are summarised in Fig. 7.

The adiabatic energy separation between the sextet and the doublet is almost zero favouring the doublet only slightly. This is consistent with the large plateau of co-existence of the two spin states obtained by Harding et al.[6]

Since this is a two-electron spin inter-conversion, two mechanisms may be envisaged: stepwise ($S = 1/2 \rightarrow S = 3/2 \rightarrow S = 5/2$) or a concerted two-electron promotion enabling direct access to the $S = 5/2$ state. The first two MECPs (²X/⁴A and ²X/⁶A) are the limiting steps and are very close in energy. These barrier heights differ by just 4.2 kJ mol⁻¹ in favour of the stepwise mechanism. This shows a picture of competition between the two spin interchange mechanisms.

However, the experimental results point to no observation of the quartet intermediate on the basis of XRD and Mössbauer data.[6] The prevalence of the concerted two-electron jump will thus be determined by less obvious factors such as lattice re-organisation and the volume of the counterion. The $S = 3/2$ intermediate (+15.8 kJ mol⁻¹) should be Jahn–Teller active which implies loss of symmetry in the lattice. Our conclusion is that no significant differentiation exists in vacuo between the several spin states of the cation.

Conclusions

Four new salts based on the [Fe(nsal₂trien)]⁺ cation were prepared, [Fe(nsal₂trien)]Cl·CH₃CH₂OH·H₂O (**1**), [Fe(nsal₂-

Fig. 6 Diagram showing the location of an MECP for the crossing of a sextet (high spin) and a doublet (low spin).

trien)]ClO₄ (**2**), [Fe(nsal₂trien)]BF₄ (**3**), and [Fe(nsal₂trien)]BPh₄ (**4**). At room temperature, the cations of these salts are HS (**2**, **3**) or mainly LS (**1**, **4**). This variability is consistent with the equilibria between the LS and HS states of the cations observed in solution at ambient temperature.

The calculated Δ_{oct} values for all the title compounds **1–6** are very similar suggesting that the different SCO behaviours are mainly determined by the supramolecular arrangements. In fact, the analysis of the intermolecular interactions in these salts shows that the rigid crystal structures, evidencing stronger interactions, either trap the HS configuration, as in **2** and **3** where the distortion of the Fe^III coordination octahedra is higher, or in the case of **1** keep the LS configuration up to higher temperatures than salts with more flexible crystal structures such as **4**, **5** or **6**. It should however be stressed that this trend observed for the title compounds may not be generalized since SCO has been observed in quite rigid structures such as in Fe–Cr Prussian blue analogues.[36] In **6**, the SCO process occurring at lower temperature is sharp while the second transition is gradual which correlates with the weakening of the contacts in the intermediate phase structure when compared to the LS phase structure.

The detailed study of the different intermolecular interactions further shows the relevance of the indirect interactions mediated by the anions and solvent molecules. The crystal packing of the series of compounds based on the [Fe(nsal₂trien)]⁺ cation is primarily determined by a pair of very strong DA NH···X hydrogen bonds (**1–3** and **6**). In compound **4**, these interactions are also strong but they are expected to give rise to a more flexible lattice since they are established with Ph groups of four different BPh₄⁻ anions (D···Ph–B–Ph···D) which are significantly larger and may accommodate a higher degree of deformation than the anions in the remaining compounds. Compound **5** shows the weakest DA, due to a pairing of the cations through strong NH···π DD interactions, leaving just one NH to establish strong DA interactions. This may explain why the onset of a SCO transition is observed in **4** and **5** while in **1–3** this is not the case. Although with strong DA interactions, compound **6** is the only one that shows a complete SCO. This may be attributed to the fact that it exhibits the weakest direct DD interactions of the whole series of the title compounds due to the tilting of the phenoxy rings of neighbouring cations in all three structures, LS, Int and HS, as explained above. On the other hand, the high cooperativity in the low-temperature process of **6** is only possible due to the efficient DAD connectivity and the rather subtle reinforcement of the weak DD interaction that is found in the Int phase.

Calculations in the gas phase have led to an estimation of the crystal splitting gap where the HS form of **6** assumes the highest value of Δ_{oct} and the LS isomer the lowest value for the set of structures studied in this report. This is consistent with the change of phase in the crystal since it demands the minimum amount of work to structurally change the bond lengths. The equilibrium ΔE_{HS-LS} energy difference is +1.1 kJ mol⁻¹ and the viability for the two-electron spin transition

having a thermal barrier of 24.9 kJ mol⁻¹ (6.0 kcal mol⁻¹) was shown to be in agreement with experimental findings.[4]

Conflicts of interest

There are no conflicts to declare.

Acknowledgements

Notes and references

1 (*a*) *Spin-Crossover Materials – Properties and Applications*, ed. M. A. Halcrow, Wiley, Chichester, 2013; (*b*) *Spin Crossover in Transition Metal Compounds I-III*, ed. A. de Meijere, K. N. Houk, H. Kessler, J.-M. Lehn, S. V. Ley, S. L. Schreiber, J. Thiem, B. M. Trost, F. Vögtle and H. Yamamoto, *Top. Curr. Chem.*, 2004, pp. 233–235.

2 H. J. Shepherd, G. Molnár, W. Nicolazzi, L. Salmon and A. Bousseksou, *Eur. J. Inorg. Chem.*, 2013, 653–661.

3 (*a*) O. Sato, J. Tao and Y. Z. Zhang, *Angew. Chem., Int. Ed.*, 2007, **46**, 2152–2187; (*b*) I. Šalitroš, N. T. Madhu, R. Boča, J. Pavlik and M. Ruben, *Monatsh. Chem.*, 2009, **140**, 695–733.

4 B. J. C. Vieira, J. T. Coutinho, I. C. Santos, L. C. J. Pereira, J. C. Waerenborgh and V. da Gama, *Inorg. Chem.*, 2013, **52**, 3845.

5 R. Pritchard, S. A. Barrett, C. A. Kilner and M. A. Halcrow, *Dalton Trans.*, 2008, 3159.

6 D. J. Harding, W. Phonsri, P. Harding, K. S. Murray, B. Moubaraki and G. N. L. Jameson, *Dalton Trans.*, 2015, **44**, 15079–15082.

7 (*a*) M. A. Halcrow, *Chem. Soc. Rev.*, 2011, **40**, 4119; (*b*) I. Nemec, R. Herchel, I. Šalitroš, Z. Trávníček, J. Moncoľ, H. Fuess, M. Ruben and W. Linert, *CrystEngComm*, 2012, **14**, 7015–7024; (*c*) D. J. Harding, P. Harding and W. Phonsri, *Coord. Chem. Rev.*, 2016, **313**, 38–61.

8 G. M. Sheldrick, *SADABS*, Bruker AXS Inc., Madison, WI, 2004.

9 *SMART and SAINT*, Bruker AXS Inc., Madison, WI, 2008.

10 A. Altomare, M. C. Burla, M. Camalli, G. Cascarano, G. Giacovazzo, A. Guagliardi, A. G. G. Moliterni, G. Polidori and R. J. Spagna, *Appl. Crystallogr.*, 1999, **32**, 115–119.

11 G. M. Sheldrick, *Acta Crystallogr., Sect. A: Found. Crystallogr.*, 2008, **64**, 112–122.

12 L. J. Farrugia and X. Wing, *J. Appl. Crystallogr.*, 2012, **45**, 849–854.

13 C. F. Macrae, I. J. Bruno, J. A. Chisholm, P. R. Edgington, P. McCabe, E. Pidcock, L. Rodriguez-Monge, R. Taylor, J. van de Streek and P. A. J. Wood, *Appl. Crystallogr.*, 2008, **41**, 466–470.

14 D. Aravena, M. Atanasov, U. Becker, M. Brehm, D. Bykov, V. G. Chilkuri, D. Datta, A. K. Dutta, D. Ganyushin, Y. Guo,

A. Hansen, L. Huntington, R. Izsak, C. Kollmar, S. Kossmann, M. Krupicka, D. Lenk, D. Liakos, D. Manganas, D. Pantazis, T. Petrenko, P. Pinski, C. Reimann, M. Retegan, C. Riplinger, T. Risthaus, M. Roemelt, M. Saitow, B. Sandhoefer, K. Sivalingam, G. Stoychev, B. Wezisla and F. Wennmohs, *ORCA v. 4.0*, Univ. Bonn, 2017; F. Neese, *Wiley Interdisc. Rev. Comput. Mol. Sci.*, 2012, **2**(1), 73–78.

15 (*a*) M. Reiher, O. Salomon and B. A. Hess, *Theor. Chem. Acc.*, 2001, **107**, 48–55; (*b*) A. D. Becke, *J. Chem. Phys.*, 1993, **98**, 5648–5652; (*c*) A. D. Becke, *Phys. Rev. A: At., Mol., Opt. Phys.*, 1988, **38**, 3098–3100; (*d*) C. Lee, W. Yang and R. G. Parr, *Phys. Rev. B: Condens. Matter Mater. Phys.*, 1988, **37**, 785–789.

16 F. Weigend and R. Ahlrichs, *Phys. Chem. Chem. Phys.*, 2005, **7**, 3297–3305.

17 (*a*) S. Kossmann and F. Neese, *Chem. Phys. Lett.*, 2009, **481**, 240–243; (*b*) F. Neese, F. Wennmohs, A. Hansen and U. Becker, *Chem. Phys.*, 2009, **356**, 98–109.

18 C. C. J. Roothaan, *Rev. Mod. Phys.*, 1960, **32**, 179–185.

19 J. N. Harvey, *Wiley Interdisc. Rev. Comput. Mol. Sci.*, 2014, **4**, 1–14.

20 S. Grimme, J. Antony, S. Ehrlich and H. Krieg, *J. Chem. Phys.*, 2010, **132**, 154104.

21 A. D. Becke and E. R. Johnson, *J. Chem. Phys.*, 2005, **123**, 154101.

22 (*a*) Y. Nishida, K. Kino and S. J. Kida, *J. Chem. Soc., Dalton Trans.*, 1987, 1957; (*b*) E. Sinn, G. Sirn, E. V. Dose, M. F. Tweedle and L. J. Wilson, *J. Am. Chem. Soc.*, 1978, **100**, 3375; (*c*) C. Faulmann, P. Á. Szilágyi, K. Jacob, J. Chahine and L. Valade, *New J. Chem.*, 2009, **33**, 1268; (*d*) S. Dorbes, L. Valade, J. A. Real and C. Faulmann, *Chem. Commun.*, 2005, 69.

23 I. C. Berdiell, R. Kulmaczewski and M. A. Halcrow, *Inorg. Chem.*, 2017, **56**, 8817.

24 (*a*) N. Bridonneau, L. Rigamonti, G. Poneti, D. Pinkowicz, A. Forni and A. Cornia, *Dalton Trans.*, 2017, **46**, 4075; (*b*) L. J. K. Cook, R. Mohammed, G. Sherborne, T. D. Roberts, S. Alvarez and M. A. Halcrow, *Coord. Chem. Rev.*, 2015, **289–290**, 2–12; (*c*) G. A. Craig, O. Roubeau and G. Aromí, *Coord. Chem. Rev.*, 2014, **269**, 13–31; (*d*) C. Bartual-Murgui, S. Vela, O. Roubeau and G. Aromí, *Dalton Trans.*, 2016, **45**, 14058; (*e*) H. Hagiwara, T. Masuda, T. Ohno, M. Suzuki, T. Udagawa and K. Murai, *Cryst. Growth Des.*, 2017, **17**, 6006–6019.

25 M. Griffin, S. Shakespeare, H. J. Shepherd, C. J. Harding, J. L. Létard, C. Desplanches, A. E. Goeta, J. A. K. Howard, A. K. Powell and V. Mereacre, *et al.*, *Angew. Chem., Int. Ed.*, 2011, **50**, 896–900.

26 Z.-Y. Li, J.-W. Dai, Y. Shiota, K. Yoshizawa, S. Kanegawa and O. Sato, *Chem. – Eur. J.*, 2013, **19**, 12948–12952.

27 K. D. Murnaghan, C. Carbonera, L. Toupet, M. Griffin, M. M. Dîrtu, C. Desplanches, Y. Garcia, E. Collet, J. F. Létard and G. G. Morgan, *Chem. – Eur. J.*, 2014, **20**, 5613–5618.

28 (*a*) N. Ortega-Villar, M. C. Muñoz and J. A. Real, *Magnetochemistry*, 2016, **2**, 16; (*b*) M. Shatruk, H. Phan, B. A. Chrisostomo and A. Suleimenova, *Coord. Chem. Rev.*, 2015, **289–290**, 62–73.

29 T. A. Ivanova, I. V. Ovchinnikov, R. R. Garipov and G. I. Ivanova, *Appl. Magn. Reson.*, 2011, **40**, 1–10.

30 W. Phonsri, D. J. Harding, P. Harding, K. S. Murray, B. Moubaraki, I. A. Gass, J. D. Cashion, G. N. L. Jameson and H. Adams, *Dalton Trans.*, 2014, **43**, 17509–17518.

31 (*a*) M. A. Spackman and J. J. McKinnon, *CrystEngComm*, 2002, **4**, 378–392; (*b*) J. J. McKinnon, D. Jayatilaka and M. A. Spackman, *Chem. Commun.*, 2007, 3814–3816; (*c*) A. V. Vologzhanina, A. S. Belov, V. V. Novikov, A. V. Dolganov, G. V. Romanenko, V. I. Ovcharenko, A. A. Korlyukov, M. I. Buzin and Y. Z. Voloshin, *Inorg. Chem.*, 2015, **54**, 5827–5838.

32 *Density Functional Theory of Atoms and Molecules*, ed. R. G. Parr and W. Yang, Oxford University Press, 1st edn, 1994.

33 J. Cano, E. Ruiz, S. Alvarez and M. Verdaguer, *Comments Inorg. Chem.*, 1998, **20**, 27–56.

34 C. Desplanches, E. Ruiz, A. Rodriguez–Fortea and S. Alvarez, *J. Am. Chem. Soc.*, 2002, **124**, 5197–5205.

35 J. N. Harvey, *Wiley Interdisc. Rev. Comput. Mol. Sci.*, 2014, **4**, 1–14.

36 E. Coronado, M. C. Gimenez-Lopez, G. Levchenko, F. M. Romero, V. Garcia-Baonza, A. Milner and M. Paz-Pasternak, Pressure-tuning of magnetism and linkage isomerism in iron(II) hexacyanochromate, *J. Am. Chem. Soc.*, 2005, **127**, 4580–4581.